Holocene turbidites record earthquake supercycles at a slow-rate plate boundary

Gueorgui Ratzov, A. Cattaneo, Nathalie Babonneau, Jacques Déverchère, K. Yelles, R. Bracene, F. Courboulex

Publisher: GSA
Journal: GEOL: Geology
DOI:10.1130/G36170.1

Holocene turbidites record earthquake supercycles at slow rate plate boundary

Gueorgui Ratzov[1,2*], Antonio Cattaneo[2], Nathalie Babonneau[1], Jacques Déverchère[1], Karim Yelles[3], Rabah Bracene[4], and Françoise Courboulex[5]

[1]Université de Brest, CNRS UMR 6538, Domaines Océaniques, IUEM, 29280 Plouzané, France

[2]IFREMER, Géosciences Marines–EDROME, 29280 Plouzané, France

[3]Centre de Recherche en Astronomie Astrophysique et Géophysique, 16006 Algiers, Algeria

[4]SONATRACH Exploration, 35000 Boumerdès, Algeria

[5]Géoazur, Université de Nice/Sophia-Antipolis, CNRS, Observatoire de la Côte d'Azur, 06560 Valbonne, France

*Current address: Géoazur, Université de Nice/Sophia-Antipolis, CNRS, Observatoire de la Côte d'Azur, 06560 Valbonne, France

ABSTRACT

Ongoing evidence for earthquake clustering calls upon records of numerous earthquake cycles to improve seismic hazard assessment, especially where recurrence times overstep historical records. We show that most turbidites emplaced at the Africa-Eurasia plate boundary off west Algeria over the past ~8 k.y. correlate across sites fed by independent sedimentary sources, requiring a regional trigger. Correlation with paleoseismic data inland and ground motion predictions support that M ~7 earthquakes have caused them. The bimodal distribution of paleo-events supports the concepts of

Publisher: GSA
Journal: GEOL: Geology
DOI:10.1130/G36170.1

earthquake supercycles and rupture synchronization between nearby faults: thirteen paleo-earthquakes underpin clusters of 3–6 events with recurrence intervals of ~300–600 yr, separated by periods of quiescence of ~1.6 k.y. without major events on other faults over the study area. This implies broad phases of strain loading alternating with phases of strain release. Our results suggest that fault slip rates are time-dependent and call upon revising conventional seismic hazard models.

INTRODUCTION

Earthquake time series reveal that rupture occurrence depends on the history of the causative fault, but also of adjacent ones (Stein, 1999; Scholz, 2010). Two main limitations however exist in outcrop study of faults: the scarce access to faults and the short time span of earthquake time series. Chronostratigraphy of earthquake-triggered turbidites provides insightful paleoquake records in subduction zones (Goldfinger et al., 2003) and helps overcoming these limitations.

Turbidite paleoseismology relies on the fact that significant seafloor shaking during large earthquakes promotes multiple and widespread turbidity currents, depositing greater sediment volumes (Goldfinger et al., 2003 and references therein) than those triggered by climatic events (Einsele et al., 1996). A widespread synchronous trigger is a key assumption for reconstructing paleo-earthquake records. Synchroneity is established by counting, dating and correlating deposits in independent channels (Goldfinger et al., 2003), basins (Gràcia et al., 2010) or sedimentary systems (Pouderoux et al., 2014).

Turbidite stratigraphy is a powerful tool to characterize the complex and multiscale seismic behavior of megathrusts and to evidence supercycles and superquakes (Goldfinger et al., 2013). However, the behavior of slow-rate plate boundaries has

Publisher: GSA
Journal: GEOL: Geology
DOI:10.1130/G36170.1

received little attention despite high seismic risks and patchy knowledge of full seismic cycles. We aim to reconstruct thousand-year-long time-series of paleoquakes that triggered largeturbidity flows in a low seismicity rate setting, and highlight the cycling of earthquakes at a slow convergence plate boundary.

REGIONAL SETTING

The Algerian margin is located at the diffuse boundary of the African plate converging at 3–6 mm yr^{-1} toward Eurasia (Stich et al., 2006). The 1954 M_s 6.7 Orléansville earthquake and the 2003 M_w 6.8 Boumerdes earthquake triggered widespread turbidity flows documented by submarine cable breaks (Heezen and Ewing, 1955; Cattaneo et al., 2012), supporting a turbidite paleoseismology approach. The area of the Orléansville and El Asnam earthquakes (Fig. 1) is a ~150-km-long margin segment where strain is located inland along northeast-southwest strike-slip faults and landward-verging thrusts and folds (Beldjoudi et al., 2011). The main active tectonic feature is the El Asnam Fault System (EAFS) forming a complex set of deep ramps connecting laterally, followed upwards by fault-propagation folds (Avouac et al., 1992). The 1954 M_s6.7 Orléansville earthquake likely occurred along the deepest ramp without breaking the surface. In contrast, the 1980 M_s 7.3 El Asnam earthquake ruptured a ~30-km-long frontal scarp (Meghraoui et al., 1988). The El Asnam earthquake did not trigger widespread turbidity currents, since no submarine cable broke offshore, except a single cable ~200 km eastward (El Robrini et al., 1985). From available surface faulting (Beldjoudi et al., 2011) and historical seismicity (Boughacha et al., 2004), whether other faults than the EAFS can produce M >6.5 earthquakes in this part of Algeria is unclear. Offshore El Asnam, the eastern continental slope is 3–4° steep, dominated by the Kramis

fan, fed by the Kramis and Khadra canyons (Fig. 1). The canyons are obliquely oriented (N170 and N090) and build an asymmetric 800-m-high levee (Babonneau et al., 2012). Westward and eastward, the slope is steeper (up to ~16°) and shows numerous slump scars and gullies. No large active faults are observed offshore.

METHODS

Scientific Rationale

To infer the seismic trigger of turbidites, we test their synchroneity in three cores collected in two independent sedimentary systems (Fig. 1; Fig. DR1 in the GSA Data Repository[1]). Core site KMDJ07 (2630 m below sea level, mbsl) is fed by turbidity flows coming from the Kramis turbidite system, whereas core KMDJ08 (2631 mbsl) samples the margin toe and collects only turbidity currents originated from the overhanging slope. To avoid any local or climatically triggered turbidites (flood, hyperpycnal flow) that usually depict short runouts (Einsele et al., 1996), we collected core PSMKS19 (2626 mbsl) in the distal part of the Kramis fan (Fig. 1). As it is close to a A.D. 1954 cable break, it stands on the path of the earthquake-triggered turbidity currents. We then compare our record with the paleoseismic one on the El Asnam fault scarp (Meghraoui et al., 1988).

Combined effects of lower sea level before ca. 8 ka and wetter conditions in the Maghreb from the Bølling-Allerød stage (14.7–12.7 ka BP) to ca. 8 k.y. B.P. (Barcena et al., 2001) favored the connection between river mouths and canyons, and the formation of hyperpycnal flows able to reach the coring sites. We thus limited our investigation to the past ~8 k.y. when the sea level was high and climate was drier and more stable, a period less favorable to the climatic triggering of large turbidity flows.

Publisher: GSA
Journal: GEOL: Geology
DOI:10.1130/G36170.1

Sediment Analyses and Dating

We measure gamma density, porosity and magnetic susceptibility each centimeter on the cores. We split them for description, photography, X-Ray imagery, magnetic susceptibility, and laser granulometry. Finally, we measure composition of major elements by X-Ray fluorescence (XRF) (Fig. 2; Figs. DR2 and DR3). Dating turbidites requires calculating the hemipelagic accumulation rate between successive ^{14}C ages dated on planktonic foraminifers (Fig. DR4) by substracting all turbidites. We calibrate the radiocarbon dates, built age/depth models, and thus calculate the age of each turbidite (OxCal software; Figs. DR5–DR7). We choose an interpolation parameter allowing heterogeneous sediment deposition to account for possible erosion at the base of each turbidite that we cannot quantify.

RESULTS AND INTERPRETATIONS

The three cores KMDJ07, KMDJ08, and PSM-KS19 show alternating light-to-dark olive beige, poorly sorted bioclastic silty clay, interpreted as background hemipelagic deposits, and dark olive gray to olive beds with a sharp, sometimes erosive silty base and a fining-upward grain-size trend. These beds are interpreted as instantaneous turbiditic deposits (Fig. 2; Figs. DR1–DR3). The top of turbidites is determined by the analysis of several proxies. In Northern Algeria, the watersheds are mainly calcareous, resulting into relatively low contrasts in carbonated content between turbidites tails and hemipelagites based on Ca/Fe ratios (biogenic vs detrital fluxes) (Fig. 2b). This limits the use of variation in magnetic susceptibility, density or geochemical composition often used for accurate identification of turbidites (Goldfinger et al., 2003; Gràcia et al., 2010). Moreover, sediment sorting (Fig. 2c) reveals normally graded

Publisher: GSA
Journal: GEOL: Geology
DOI:10.1130/G36170.1

turbidites with a coarse base (up to 1000 μm) fining upwards to silts and clays. The grain size distribution supports well-sorted deposits. Contrastingly, most hemipelagites are unsorted and show a plateau for grain size comprised between ~30 and >300 μm associated to biogenic particles (Fig. 2c). This criterion appears more reliable for discriminating turbidites from hemipelagites when the compositional contrast is low (Ratzov et al., 2010). Where discrimination remains uncertain (e.g., sediment mixing by bioturbation), we consider the interval as an uncertainty included in the age model (Fig. 2; Figs. DR2 and DR3).

Turbidites may be stacked without intervening hemipelagites in proximal cores KMDJ07 and KMDJ08. Such stacks may reflect: (1) simultaneous slope failures during an earthquake, (2) large aftershocks or earthquakes occurring closely in space and time, (3) pulses and flow discontinuities in the turbidity current (Van Daele et al., 2013) or (4) seafloor erosion of hemipelagites by the coarse fraction of the subsequent turbidite (Goldfinger et al., 2003). Since we hardly discriminate among these scenarii, we consider a single trigger when stacks contain no hemipelagites, and multiple triggers where the presence of hemipelagites is unclear.

We define an event (E) as a turbidite or a stack of turbidites that either corresponds to a historical earthquake or is synchronous in at least two cores. We identify 13 events based on turbidite correlation with overlapping age error bars across two or three cores (Figs. 2 and 3). Although the error bars of events may overlap, the stratigraphy of deposits allows establishing the number of events. Seven events are retrieved in all cores (E3, E5, E9, E10, E11, E12, and E13), five correlate across two

Publisher: GSA
Journal: GEOL: Geology
DOI:10.1130/G36170.1

cores (E2 and E4 collected in the same system, E6, E7, and E8), and only two turbidites are single ones: T1 in core PSMKS19 (E1) and T10 in core KMDJ07 (Fig. 2a).

Ground motion prediction equations applied to our case study show that M >6.5 earthquakes are required to produce a peak ground acceleration (PGA) sufficient to promote slope failures (Fig. 4; Fig. DR8). Our study should therefore trace the cycling of M >6.5 earthquakes occurring approximately within the area mapped in Figure 1.

DISCUSSION AND CONCLUSION

From Turbidites to Paleo-Earthquakes

The greater amount of turbidites in more proximal cores (Fig. DR1) suggests that turbidites in our cores are not linked to climatic events (floods, hyperpycnal flows) that usually depict short runouts. Instead, the clear synchroneity of at least seven groups of turbidites supports a regional trigger that we interpret as coseismic. Although visible in a single core, turbidite T1 of core PSMKS19 has an error bar (0–460 yr) that includes the age of the 1954 Orléansville earthquake and is located near a cable break (Heezen and Ewing, 1955). As no large (M >6.5) historical events occurred in the area during the 0–460 yr time span (Boughacha et al., 2004), T1 likely corresponds to the 1954 earthquake. The lack of events E1 in cores KMDJ07 and KMDJ08, and E2 in core KMDJ07, likely results from the loss of the uppermost deposits in the piston corer. Conversely, the lack of turbidites coeval with T10 in Core KMDJ07 cannot be caused by sampling limitations. Because T10 occurs ~500 yr after the previous earthquake, the slope was most likely reloaded with sediments, thus the lack of coeval record in other cores supports that T10 is local and not triggered by a large earthquake.

Publisher: GSA
Journal: GEOL: Geology
DOI:10.1130/G36170.1

The strongest argument to interpret the turbidites as coseismic is their correlation with independent paleoseismic data inland (Sumner et al., 2013), here, the El Asnam fault scarp, the greatest fault in the area. At least eight out of nine paleoquakes are coeval with the submarine record within their error bars (all events except E7, Fig. 3). This clear correlation suggests that ruptures on the El Asnam fault triggered these turbidites. However, other faults in the area may have triggered the turbidites in case they ruptured almost synchronously (i.e., within few decades) with the El Asnam paleoquakes. Indeed, although the error bar of Event E1 overlaps both 1954 and 1980 earthquakes, only the first one triggered turbidity flows in the area (Heezen and Ewing, 1955). Sediment prone to failure was probably flushed during the earlier earthquake, thus lowering the probability of a subsequent failure. Similarly, the slight asynchrony of Event E7 with the El Asnam paleo-earthquake (<100 yr) may result from bursts of activity on nearby faults. Therefore, it is impossible to assign a turbidite to a specific fault segment, and the number of large earthquakes may exceed the number of turbidites found (i.e., a single turbidite may hide multiple earthquakes). Still, the nine ruptures identified on the El Asnam fault scarp remarkably match the nine widespread turbidites deposited within very short time spans. Turbidites triggered by earthquakes from active faults located in other regions (e.g., the Iberian margin) have no chance to reach our area, given (1) the large distance (>250 km) of our coring sites to canyons and major faults of Iberia (Gràcia et al., 2006), and (2) the depth of coring, significantly less than the deepest basin floor (Babonneau et al., 2012).

Earthquake Recurrences and Supercycles

Publisher: GSA
Journal: GEOL: Geology
DOI:10.1130/G36170.1

Although the turbidite record is incomplete for earthquakes occurring closely in time (a few decades), the 13 paleo-events identified define three clusters of seismicity (Fig. 3): C1 (4 events in 1800 ± 250 yr), C2 (3 events in 850 ± 260 yr), and C3 (6 events in 1650 ± 400 yr). The distribution is bimodal: the 3 clusters depict mean Recurrence Intervals (RI) of 0.3 ± 0.2 (C3), 0.4 ± 0.2 (C2), and 0.6 ± 0.4 ka (C1) and are separated by two Quiescence periods Q1 and Q2 of 1625 ± 490 yr and 1575 ± 580 yr, respectively (Fig. 3). This distribution suggests 3–4 k.y.-long patterns including clusters of 3 to 6 events and periods without major events inbetween. This variability in earthquake recurrence is akin to the concept of "supercycles" suggested in subduction zones (Goldfinger et al., 2013). Interestingly, similar quiescence periods are found in the southwest Iberian margin (Gràcia et al., 2010) and in central Italy (Benedetti et al., 2013), where slip rates are low. This concept supports alternation of broad phases of strain loading and shorter phases of strain release and implies that fault slip rates are time dependent (Friedrich et al., 2003; Benedetti et al., 2013). Note also that the mean RI in clusters rises progressively (C3: 305 yr; C2: 430 yr; C1: 580 yr; Fig. 3), suggesting that strain rates may change through time.

Earthquake Synchrony

Fault interactions have proved to promote or delay fault activity by stress transfer, sometimes leading to synchronization between fault segments (Scholz, 2010). If slope sediments are prone to failure, turbidites record the activity of any neighboring fault able to cause earthquakes strong enough to trigger turbidity currents (Fig. 4). The cluster/quiescence pattern found here supports the idea that the seismogenic segments (EAFS and other large faults in the area) are in synchrony, at least at the scale of the

study region (~100 × 100 km, Fig. 1). Knowledge of long-term cycling in the rupture pattern (here, two complete supercycles; Fig. 3) is important since it reveals phases of strain release and loading, therefore a given elapsed time after a clustering period would not necessarily mean a higher hazard. This result thus modifies the probability models of earthquake recurrence (Gomberg et al., 2005) and helps improve seismic hazard assessments.

ACKNOWLEDGMENTS

We thank GENAVIR for their assistance during the MARADJA and PRISME cruises, and Algerian authorities for permits and logistical supply. IFREMER and the Conseil Général du Finistère funded G. Ratzov's grant. LabexMER (ANR-10-LABX-19-01) supported part of the analyses. CNRS-INSU Artemis Program provided ^{14}C dates. We thank J.Y. Collot, M.A. Gutscher and D. Pantosti for fruitful discussions, L.McNeill, A. Polonia and four anonymous reviewers for thorough comments.

REFERENCES CITED

Akkar, S., and Bommer, J.J., 2010, Empirical Equations for the Prediction of PGA, PGV, and Spectral Accelerations in Europe, the Mediterranean Region, and the Middle East: Seismological Research Letters, v. 81, p. 195–206, doi:10.1785/gssrl.81.2.195.

Avouac, J.-P., Meyer, B., and Tapponnier, P., 1992, On the growth of normal faults and the existence of flats and ramps along the El Asnam active fold and thrust system: Tectonics, v. 11, p. 1–11, doi:10.1029/91TC01449.

Babonneau, N., Cattaneo, A., Savoie, B., Barjavel, G., Déverchère, J., and Yelles, K., 2012, Discovery of the Kramis fan offshore Algeria: the role of sediment waves in turbiditic levee growth: AAPG SEPM Special Publication, v. 99, p. 293–308.

227 Barcena, M.A., Cacho, I., Abrantes, F., Sierro, F.J., Grimalt, J.O., and Flores, J.A., 2001,
228 Paleoproductivity variations related to climatic conditions in the Alboran Sea
229 (western Mediterranean) during the last glacial, interglacial transition: the diatom
230 record: Palaeogeography, Palaeoclimatology, Palaeoecology, v. 167, p. 337–357,
231 doi:10.1016/S0031-0182(00)00246-7.
232 Beldjoudi, H., Delouis, B., Heddar, A., Nouar, O.B., and Yelles Chaouche, A., 2011, The
233 Tadjena Earthquake (Mw=5.0) of December 16, 2006 in the Cheliff Region
234 (Northern Algeria): Waveform Modelling, Regional Stresses, and Relation with the
235 Boukadir Fault: Pure and Applied Geophysics, v. 169, p. 677–691,
236 doi:10.1007/s00024-011-0337-8.
237 Benedetti, L., Manighetti, I., Gaudemer, Y., Finkel, R., Malavieille, J., Pou, K., Arnold,
238 M., Aumaître, G., Bourlès, D., and Keddadouche, K., 2013, Earthquake synchrony
239 and clustering on Fucino faults (Central Italy) as revealed from in situ ^{36}Cl exposure
240 dating: Journal of Geophysical Research, v. 118, p. 4948–4974.
241 Boughacha, M.S., Ouyed, M., Ayadi, A., and Benhallou, H., 2004, Seismicity and
242 seismic hazard mapping of northern Algeria: Map of Maximum Calculated
243 Intensities (MCI): Journal of Seismology, v. 8, p. 1–10,
244 doi:10.1023/B:JOSE.0000009513.11031.43.
245 Cattaneo, A., Babonneau, N., Ratzov, G., Dan, G., Yelles, K., Bracene, R., Mercier de
246 Lepinay, B., Boudiaf, A., and Déverchère, J., 2012, Searching for the seafloor
247 signature of the 21 May 2003 Boumerdes earthquake offshore central Algeria:
248 Natural Hazards and Earth System Sciences, v. 12, p. 2159–2172,
249 doi:10.5194/nhess-12-2159-2012.

Einsele, G., Chough, S.K., and Shiki, T., 1996, Depositional events and their records An introduction: Sedimentary Geology, v. 104, p. 1–9, doi:10.1016/0037-0738(95)00117-4.

El-Robrini, M., Genesseaux, M., and Mauffret, A., 1985, Consequences of the El Asnam Earthquake: Turbidity Currents and Slumps on the Algerian Margin (Western Mediterranean): Geo-Marine Letters, v. 5, p. 171–176, doi:10.1007/BF02281635.

Friedrich, A., Wernicke, B.P., Niemi, N.A., Bennett, R.A., and Davis, J.L., 2003, Comparison of geodetic and geologic data from the Wasatch region, Utah, and implications for the spectral character of Earth deformation at periods of 10 to 10 million years: Journal of Geophysical Research, v. 108, B4, p. 2199, doi:10.1029/2001JB000682.

Goldfinger, C., Nelson, C.H., Johnson, J.E., and Party, S.S., 2003, Holocene earthquake records from the Cascadia subduction zone and northern San Andreas Fault based on precise dating of offshore turbidites: Annual Review of Earth and Planetary Sciences, v. 31, p. 555–577, doi:10.1146/annurev.earth.31.100901.141246.

Goldfinger, C., Ikeda, Y., Yeats, R.S., and Ren, J., 2013, Superquakes and Supercycles: Seismological Research Letters, v. 84, p. 24–32, doi:10.1785/0220110135.

Gomberg, J., Belardinelli, M.E., Cocco, M., and Reasenberg, P., 2005, Time-dependent earthquake probabilities: Journal of Geophysical Research, v. 110, p. B05S04, doi:10.1029/2004JB003405.

Gràcia, E., et al., 2006, Active faulting offshore SE Spain (Alboran Sea): Implications for earthquake hazard assessment in the Southern Iberian Margin: Earth and Planetary Science Letters, v. 241, p. 734–749, doi:10.1016/j.epsl.2005.11.009.

Gràcia, E., Vizcaino, A., Escutia, C., Asioli, A., Rodes, A., Pallas, R., Garcia Orellana, J., Lebreiro, S., and Goldfinger, C., 2010, Holocene earthquake record offshore Portugal (SW Iberia): testing turbidite paleoseismology in a slow convergence margin: Quaternary Science Reviews, v. 29, p. 1156–1172, doi:10.1016/j.quascirev.2010.01.010.

Heezen, B.C., and Ewing, M., 1955, Orléansville earthquake and turbidity currents: AAPG Bulletin, v. 39, p. 2505–2514.

Meghraoui, M., Jaegy, R., Lammali, K., and Albarède, F., 1988, Late Holocene earthquake sequences on the El Asnam (Algeria) thrust fault: Earth and Planetary Science Letters, v. 90, p. 187–203, doi:10.1016/0012-821X(88)90100-8.

Pouderoux, H., Proust, J.-N., and Lamarche, G., 2014, Submarine paleoseismology of the northern Hikurangi subduction margin of New Zealand as deduced from Turbidite record since 16ka: Quaternary Science Reviews, v. 84, p. 116–131, doi:10.1016/j.quascirev.2013.11.015.

Ratzov, G., Collot, J.Y., Sosson, M., and Migeon, S., 2010, Mass transport deposits in the northern Ecuador subduction trench: Result of frontal erosion over multiple seismic cycles: Earth and Planetary Science Letters, v. 296, p. 89–102, doi:10.1016/j.epsl.2010.04.048.

Scholz, C.H., 2010, Large Earthquake Triggering, Clustering, and the Synchronization of Faults: Bulletin of the Seismological Society of America, v. 100, p. 901–909, doi:10.1785/0120090309.

295 Stein, R.S., 1999, The role of stress transfer in earthquake occurrence: Nature, v. 402,
296 p. 605–609, doi:10.1038/45144.
297 Stich, D., Serpelloni, E., de Lis Mancilla, F., and Morales, J., 2006, Kinematics of the
298 IberiaMaghreb plate contact from seismic moment tensors and GPS observations:
299 Tectonophysics, v. 426, p. 295–317, doi:10.1016/j.tecto.2006.08.004.
300 Sumner, E.J., Siti, M.I., McNeill, L.C., Talling, P.J., Henstock, T.J., Wynn, R.B.,
301 Djajadihardja, Y.S., and Permana, H., 2013, Can turbidites be used to reconstruct a
302 paleoearthquake record for the central Sumatran margin?: Geology, v. 41, p. 763–
303 766, doi:10.1130/G34298.1.
304 Van Daele, M.E., Cnudde, V., Duyck, P., Pino, M., Urrutia, R., and de Batist, M., 2013,
305 Multidirectional, synchronously triggered seismoturbidites and debrites revealed by
306 X-ray computed tomography (CT): Sedimentology, v. 61, p. 861–880,
307 doi:10.1111/sed.12070.
308

Publisher: GSA
Journal: GEOL: Geology
DOI:10.1130/G36170.1

309

310 **FIGURE CAPTIONS**

311 Figure 1. Morphostructural map of the northwestern Algerian margin. Capsule: Arrow is
312 the Africa/Eurasia convergence inferred from GPS (Stich et al., 2006). Map: Black lines
313 onland are the active fault network, double arrows are folds (Beldjoudi et al., 2011).
314 Focal mechanisms of the 1954 and 1980 earthquakes are from Avouac et al. (1992).
315 Offshore, isobaths represent 500 m. Red lines are submarine cables, stars are the breaks
316 after the 1954 earthquake (after Heezen and Ewing, 1955). Color circles are sedimentary
317 cores used in this study.

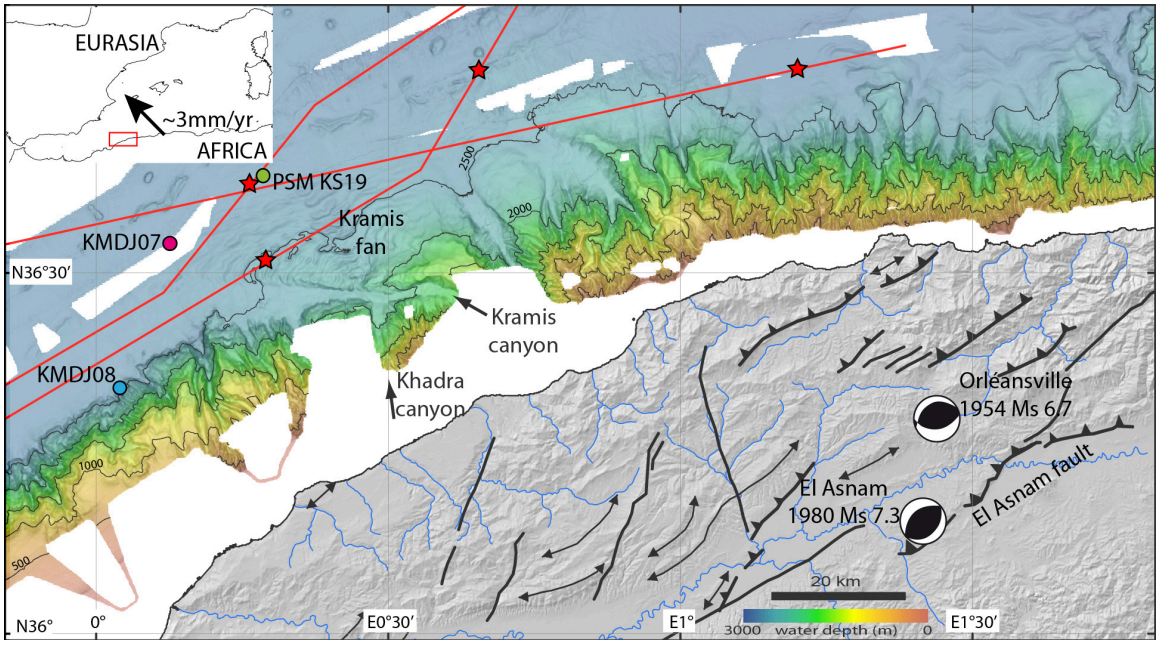

318

319

Publisher: GSA
Journal: GEOL: Geology
DOI:10.1130/G36170.1

Figure 2. Synthetic logs of the cores used for turbidite correlations depicting interpretation from turbidite in each core (Tx) to widespread events (Ex) where the turbidites are correlated across numerous cores. Gray layer outlines the uncertainties on identifying the precise turbidites boundaries. Deposits are discriminated based on Photo, X-ray pictures, magnetic susceptibility, density, XRF (B), and sediment sorting (C).

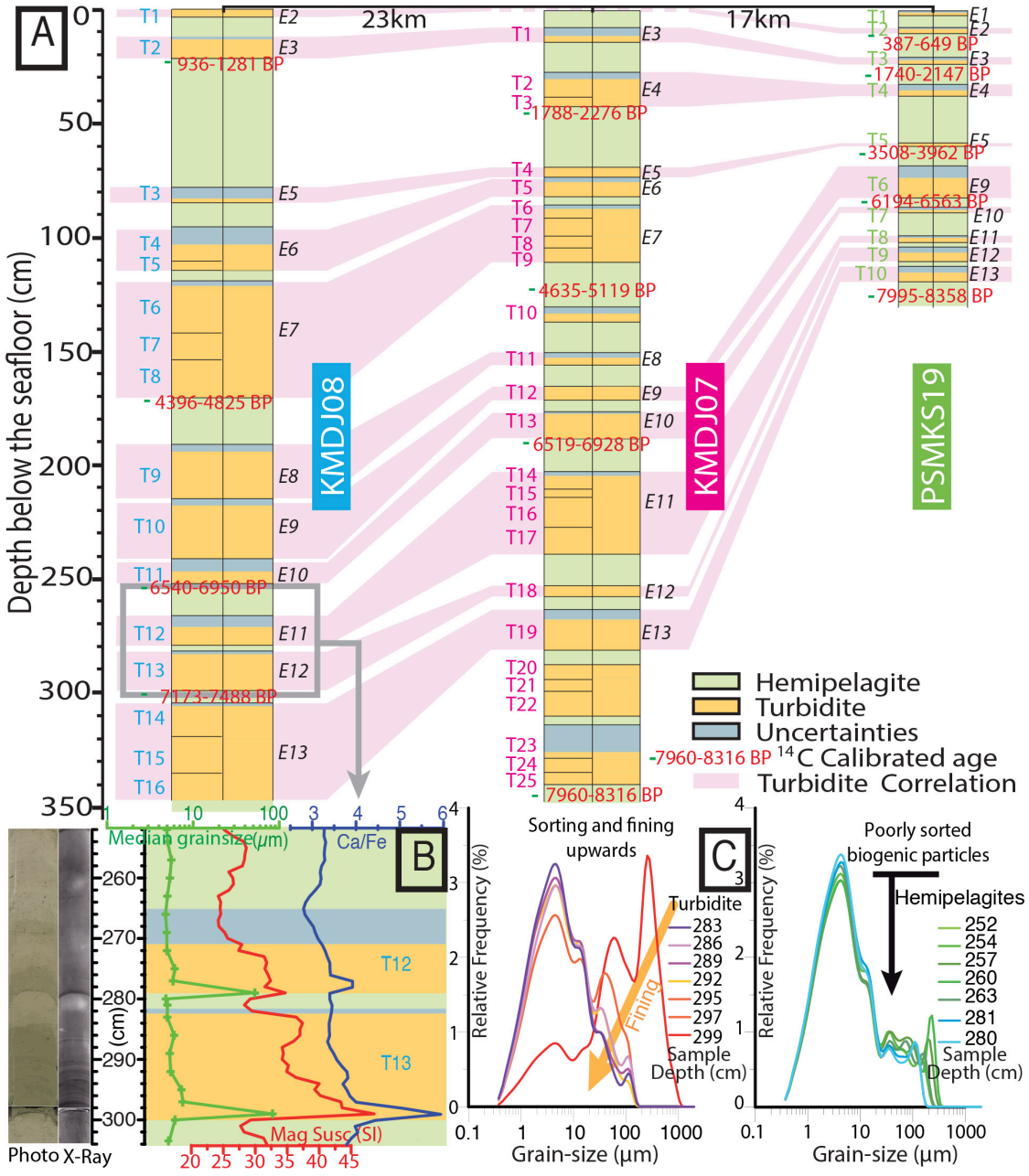

Publisher: GSA
Journal: GEOL: Geology
DOI:10.1130/G36170.1

Figure 3. Correlations between ages of events recorded in each core (color lines) and the paleoquake chronology reconstructed across the El Asnam fault (Meghraoui et al., 1988). Purple stripes outline the intersection of the error bars of turbidite ages, thus the probability age of earthquake triggering.

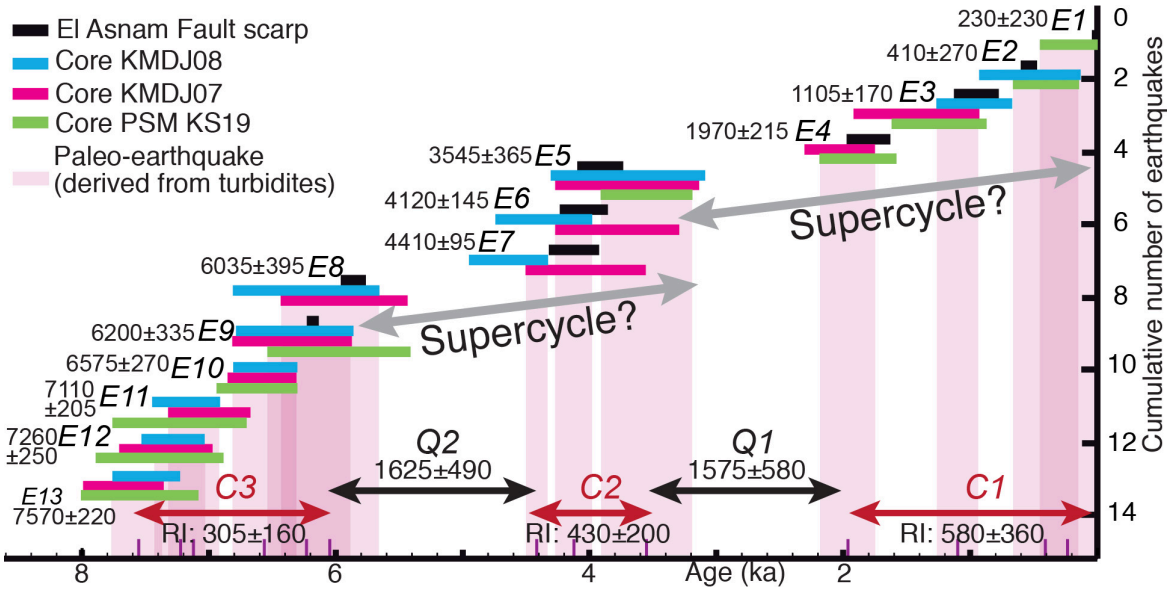

Publisher: GSA
Journal: GEOL: Geology
DOI:10.1130/G36170.1

Figure 4. Mean Peak Ground Acceleration (PGA) predicted for historical earthquakes, felt in the area of submarine canyon heads where sediment turbidity flows likely originate. PGA is calculated with empirical equations (Akkar and Bommer, 2010) for rock sites. Color stripes outline the PGA caused by M_w 6.0 ± σ and M_w 7.5 ± σ earthquakes (Fig. DR8 [see footnote 1] for further details). Geotechnical analyses of the sediment cover show that slope should fail at 0.1 g PGA.

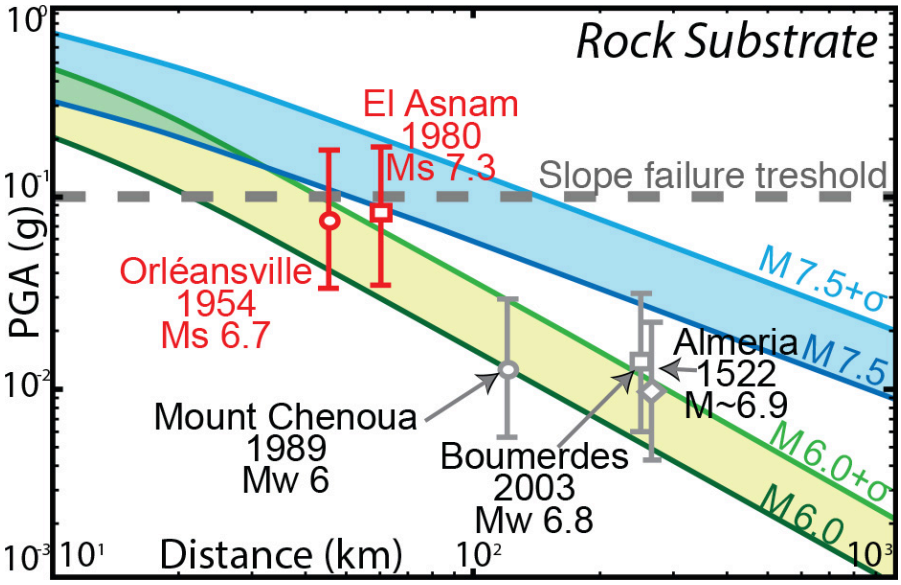

[1]GSA Data Repository item 2015xxx, xxxxxxxx, is available online at www.geosociety.org/pubs/ft2014.htm, or on request from editing@geosociety.org or Documents Secretary, GSA, P.O. Box 9140, Boulder, CO 80301, USA.

DR1: Detailed bathymetric map of the study area, sites of all the cores initially available for the paleoseismic investigation and synthetic lithologic logs of the cores. On the map, yellow circles show the location of cores, red stars are the locations of cable breaks after the 1954 M_S6.7 Orléansville earthquake. On the lithologic logs, the red rectangles show the core sections used in the study. Sedimentological analyses are detailed in SM2.

The coring strategy was established in order to (1) collect turbidites originated from independent sedimentary system to test synchroneity and infer a regional trigger of turbidites, (2) obtain a record with amounts of datable hemipelagic deposits between turbidites, (3) avoid climatically triggered turbidites, and (4) collect turbidites associated at least to the 1954 Earthquake, thus located close to the cable breaks,

This figure shows encountered issues while establishing a coring strategy for a turbidite paleoseismology investigation:

A) No datable hemipelagic deposits: For example, cores KMDJ24 and KMDJ22 did not contain any intervening hemipelagites between turbidites thus discarding dating possibilities. Indeed, these two cores are most probably too axially located compared to the sediment transport axis. Turbidity currents at these sites are too energetic, thus eroding any intervening deposits. Moreover, these two cores are also likely too proximally located, contain much more turbidites than the distal cores, and probably record flood- or storm-triggered turbidites. More generally, all the cores contain a greater amount of turbidites without intervening hemipelagites during the Last Glacial Maximum and the sea-level rise, and probably record climatic events. We therefore discarded cores KMDJ22, KMDJ24, and the periods before ~8ka on all the other cores.

B) Incomplete turbidite record: Core KMDJ23 was collected on a levee of the channel in order to avoid basal erosion by turbidity currents and climatically-driven turbidites. Unfortunately, turbidites in this core are scarce, very fine grained and difficult to identify. The core most likely contains an incomplete turbidite record and was discarded for detailed investigation.

C) Missing core tops: Loss of the uppermost deposits may occur with a piston corer as exemplified by cores KMDJ06 and PSMKS20. Although located in independent sedimentary systems and showing a good alternation of turbidites and hemipelagites, ^{14}C datings near the top of the cores show that ~6kyr and ~10kyr are missing respectively. We therefore discarded these two cores.

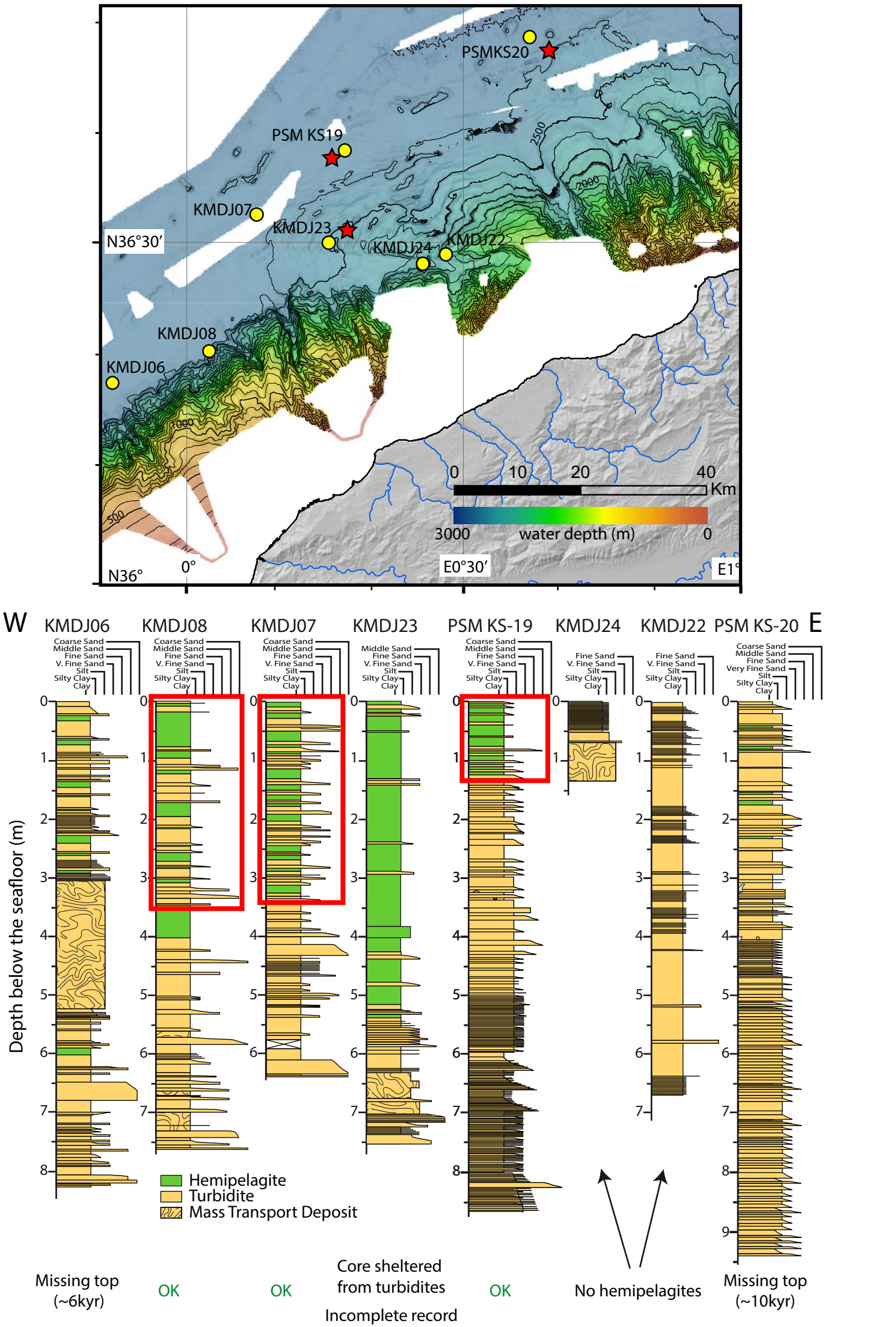
PSMKS20
PSM KS19
KMDJ07
KMDJ23
KMDJ24
KMDJ22
KMDJ08
KMDJ06
N36°30′
N36°
0°
E0°30′
E1°
2500
2000
1000
500
0 10 20 40 Km
3000 water depth (m) 0
W
E
KMDJ06
KMDJ08
KMDJ07
KMDJ23
PSM KS-19
KMDJ24
KMDJ22
PSM KS-20
Depth below the seafloor (m)
Hemipelagite
Turbidite
Mass Transport Deposit
Missing top (~6kyr)
OK
OK
Core sheltered from turbidites
Incomplete record
OK
No hemipelagites
Missing top (~10kyr)

DR2: Detailed view of cores KMDJ08, KMDJ07, and PSMKS19. Turbidites and hemipelagites were discriminated based on visual description, X-Ray photography, Magnetic Susceptibility, Gamma Density, Ca/Fe ratios, and granulometry.

X Ray photography was performed using the SCOPIX system at the University of Bordeaux I (Migeon et al., 1999); Magnetic Susceptibility was performed using a hand operating, high resolution, BARTINGTON surface sensor with 10s acquisitions; Gamma Density was performed on unopened cores with a GEOTEK Multi Sensor Core Logger; Semi-quantitative major elements composition was performed using a X-Ray Fluorescence Core Scanner. All these analyses were acquired at a step of 1cm. Finally, granulometry was acquired using a COULTER LS230 Laser Granulometer, at a step ranging between one and five centimeters depending on the homogeneity of deposits.

We outlined the portions where uncertainties on the discrimination of deposits remain, such as within bioturbated sediment.

The correlation from site to site was based on the age of each turbidite or stack of turbidites. Please refer to SM3 to SM6 for details on ^{14}C datings and establishment of age models.

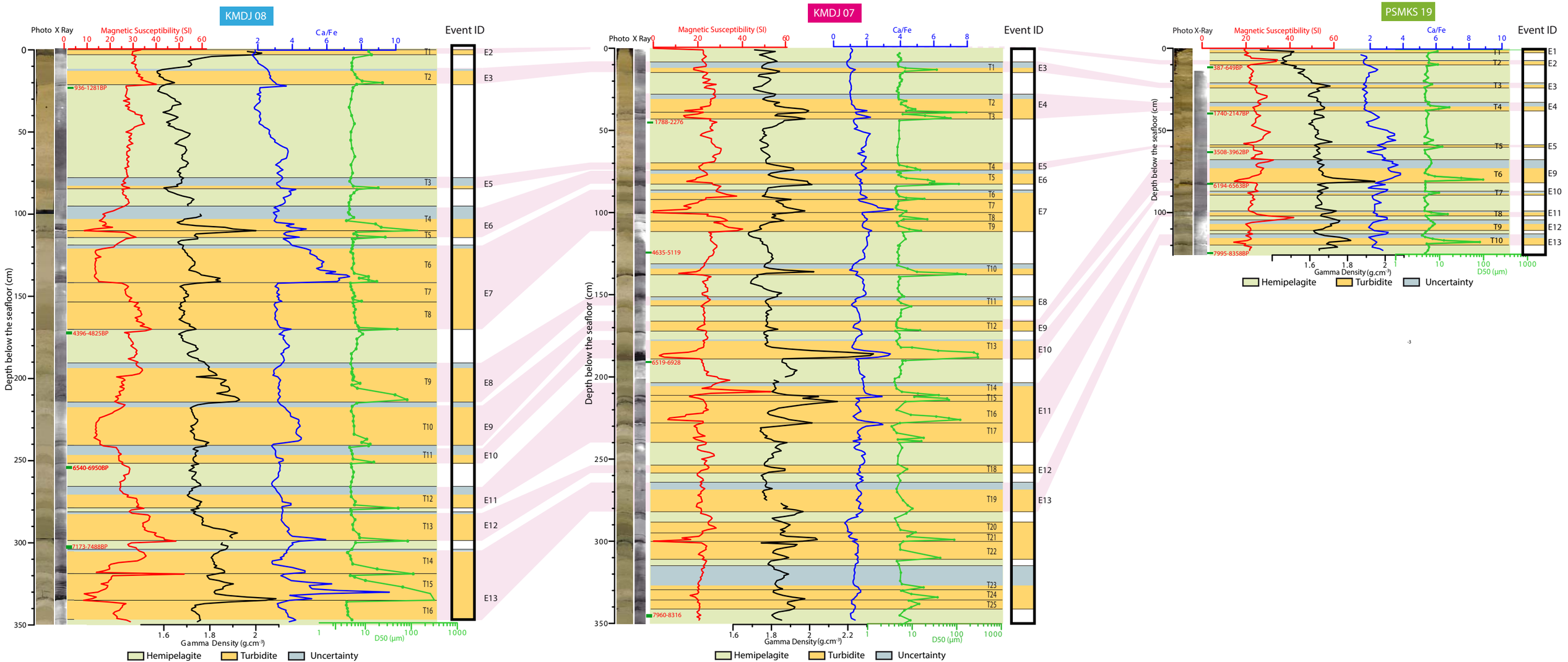
KMDJ 08
Photo X Ray
Magnetic Susceptibility (SI)
Ca/Fe
Event ID
Depth below the seafloor (cm)
936-1281BP
4396-4825BP
6540-6950BP
7173-7488BP
T1
T2
T3
T4
T5
T6
T7
T8
T9
T10
T11
T12
T13
T14
T15
T16
E2
E3
E5
E6
E7
E8
E9
E10
E11
E12
E13
Gamma Density (g.cm-3)
D50 (µm)
KMDJ 07
1788-2276
4635-5119
6519-6928
7960-8316
T17
T18
T19
T20
T21
T22
T23
T24
T25
E4
PSMKS 19
387-649BP
1740-2147BP
3508-3962BP
6194-6563BP
7995-8358BP
E1
Hemipelagite
Turbidite
Uncertainty

DR3: Detailled grain-size histograms of all the analyses performed on cores KMDJ08, KMDJ07, and PSMKS19. Analyses were performed at 1 to 5 cm intervals depending on the variation of sedimentary facies. Each sample was collected with a 0.5 cm-large spatula, and analysed with a COULTER LS230 Laser Diffraction Particle Size Analyser. Facies and grain-size were interpreted using multiple proxies: visual identification, Xray radioscopy, gamma density, magnetic susceptibility, and XRF (SM2).
These analyses aim to accurately point the boundaries between hemieplagites and turbidites (see main text for details). As the difference between turbidite tails and hemipelagites may not be obvious, we systematically performed a serie of measurement from base to top of turbidite to infer the subtle evolution of grainsize during fining upwards, and pointed out where the grainsize signature changed. The hemipelagic deposit aver usually less sorted in these cores, characterized by a plateau in grainsize for ~30-300µm (see main text). However, hemipelagites properties may vary, and where sorting was less obvious, the interpretation was helped by the other proxies. We considered unclear intervals as uncertainties.

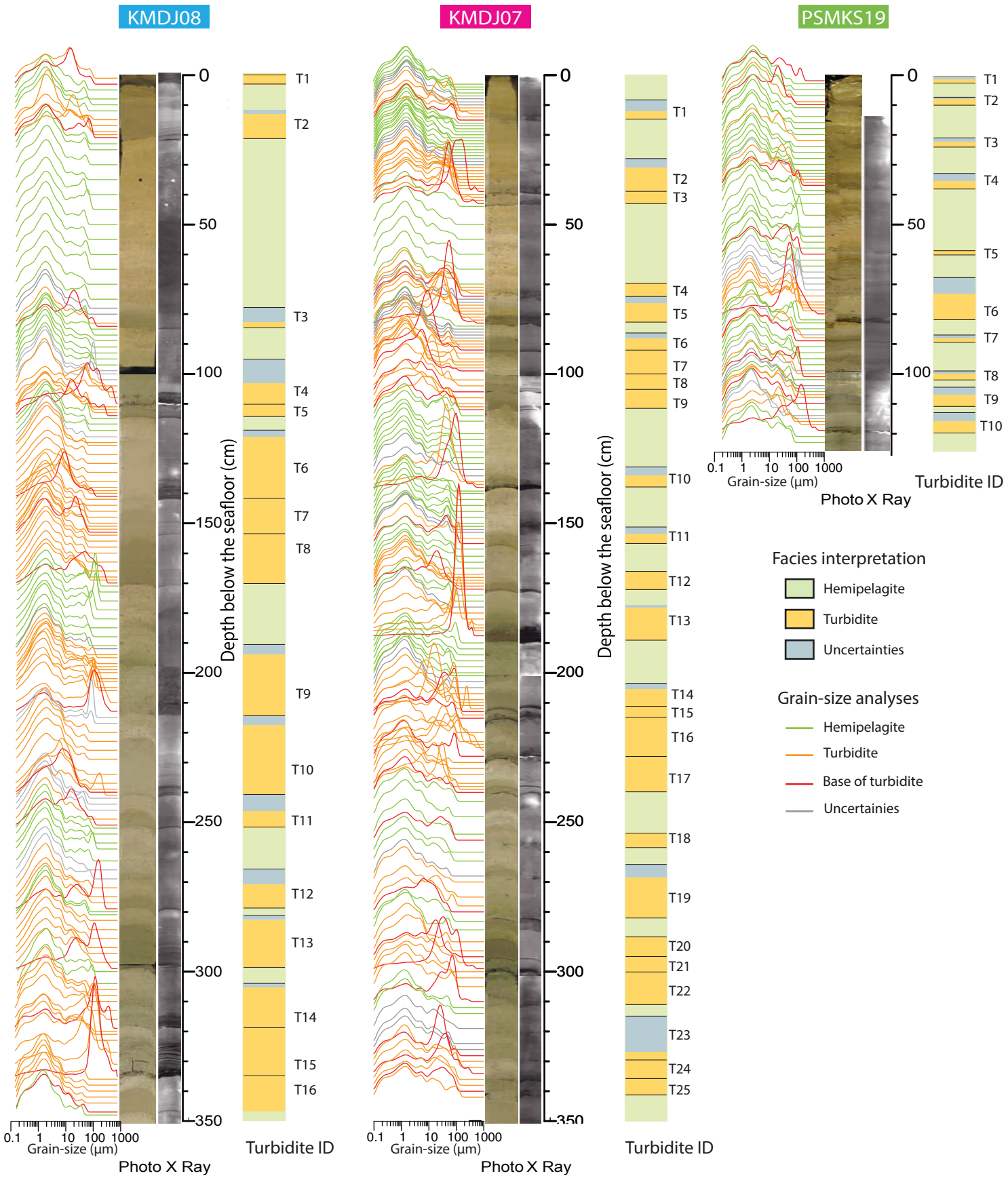
KMDJ08
KMDJ07
PSMKS19
Depth below the seafloor (cm)
0
50
100
150
200
250
300
350
T1
T2
T3
T4
T5
T6
T7
T8
T9
T10
T11
T12
T13
T14
T15
T16
T17
T18
T19
T20
T21
T22
T23
T24
T25
0.1 1 10 100 1000
Grain-size (µm)
Photo X Ray
Turbidite ID
Facies interpretation
Hemipelagite
Turbidite
Uncertainties
Grain-size analyses
Hemipelagite
Turbidite
Base of turbidite
Uncertainies

DR4: Radiocarbon dates used to construct the age model. We performed radiocarbon dating using 13 samples of 1 to 2 cm-thick slices of hemipelagic sediment. We handpicked >10mg of >150µm-diameter foraminifers per date. We preferentially used species *Globigerinoides Ruber* and *Globigerinoides Sacculifer* because they are common species living in shallow waters (0-50m), and completed with *Globigerinoides Bulloides* (0-200m) or mixed planktonic foraminifers to reach 10mg when needed. ^{14}C AMS dating were then processed at the CAIS Lab (University of Georgia – Sample codes UGAMS) or at the French national facility ARTEMIS (sample codes SacA). To obtain accurate dating, we calibrated the radiocarbon ages with the OxCal software (Ramsey, 2008) using the Marine09 curve. In the Western Mediterranean sea offshore Algeria, as marine radiocarbon reservoir may vary a lot (Reimer and McCormac, 2002), we used a standard $\Delta R=0$ value, and an extreme $\Delta R=161\pm40$yr measured offshore Algeria (Reimer and McCormac, 2002), then considered the whole age interval as an uncertainty bar $\Delta R=101\pm100$yr.

Core	Lat (dec °)	Lon (dec °)	Water depth (m)	Core length (m)	AMS Lab reference	Depth in the core (cm)	Foraminifer species	Radiocarbon age (yr ± 1σ)	Calibrated age (cal yr BP / 2σ)
KMDJ08	36.3362	0.0462	2631	7.65	UGAMS 9291	23	*G. ruber, G. sacculifer, G. bulloides*	1660 ± 25	936-1281
					UGAMS 9292	171	*G. ruber, G. sacculifer, G. bulloides*	4540 ± 25	4396-4825
					UGAMS 9293	253	*G. ruber, G. sacculifer, G. bulloides*	6390 ± 25	6540-6950
					UGAMS 9294	303	*G. ruber, G. sacculifer, G. bulloides*	6910 ± 25	7173-7488
KMDJ07	36.5403	0.1267	2630	6.68	UGAMS 8785	45	*G. ruber, G. sacculifer, G. bulloides*	2590 ± 25	1788-2276
					SacA 29350	124-125	*G. ruber, G. sacculifer*	4745 ± 30	4635-5119
					UGAMS 8786	190	Mixed Planctonic Foraminifers	6370 ± 25	6516-6928
					UGAMS 8788	345	Mixed Planctonic Foraminifers	7770 ± 25	7960-8316
PSM KS19	36.6340	0.2863	2626	8.65	UGAMS 8782	11	*G. ruber, G. sacculifer, G. bulloides*	1020 ± 25	387-649
					UGAMS 8783	39	*G. ruber, G. sacculifer, G. bulloides*	2430 ± 25	1740-2147
					SacA 29351	63-64	*G. ruber, G. sacculifer*	3885 ± 30	3508-3962
					SacA 21669	82	*G. ruber, G. sacculifer*	6045 ± 30	6194-6563
					UGAMS 8784	127	Mixed Planctonic Foraminifers	7820 ± 25	7995-8358

DR5-DR7: Age / Depth models used to calculate the age of each turbidite / event in cores KMDJ08, KMDJ07, and PSMKS19.

Because each turbidite is located few to tens centimeters away from dated hemipelagic samples, it is necessary to interpolate / extrapolate the time span of each intervening hemipelagic interval. We used a Bayesian model of deposition *P_sequence* implemented in the OxCal software (Ramsey, 2008). The program considers hemipelagic sedimentation as a random process, and takes into account variation in the sedimentation rates. Thus, uncertainties increase with distance from calibrated age samples. The *k* value determines the regularity of sedimentation rates: a high value (1 or more) considers an almost homogeneous deposition. Erosion is observed at the base of numerous turbidites, and we cannot quantify it. We therefore intentionally chose a low value of *k* (0.1) in order to reflect high variability of sedimentation rates and account for basal erosion.

For each core, we computed two age/depth models: **(A)** considering minimum turbidite thickness were uncertainties on the boundary between hemipelagites existed, and **(B)** considering maximum turbidite thickness. As the modeled turbidite age distribution could differ between the two models we considered the sum of the distributions as an error bar for each turbidite **(C)**. The bars below each age distribution corresponds to 2 sigma.

KMDJ08

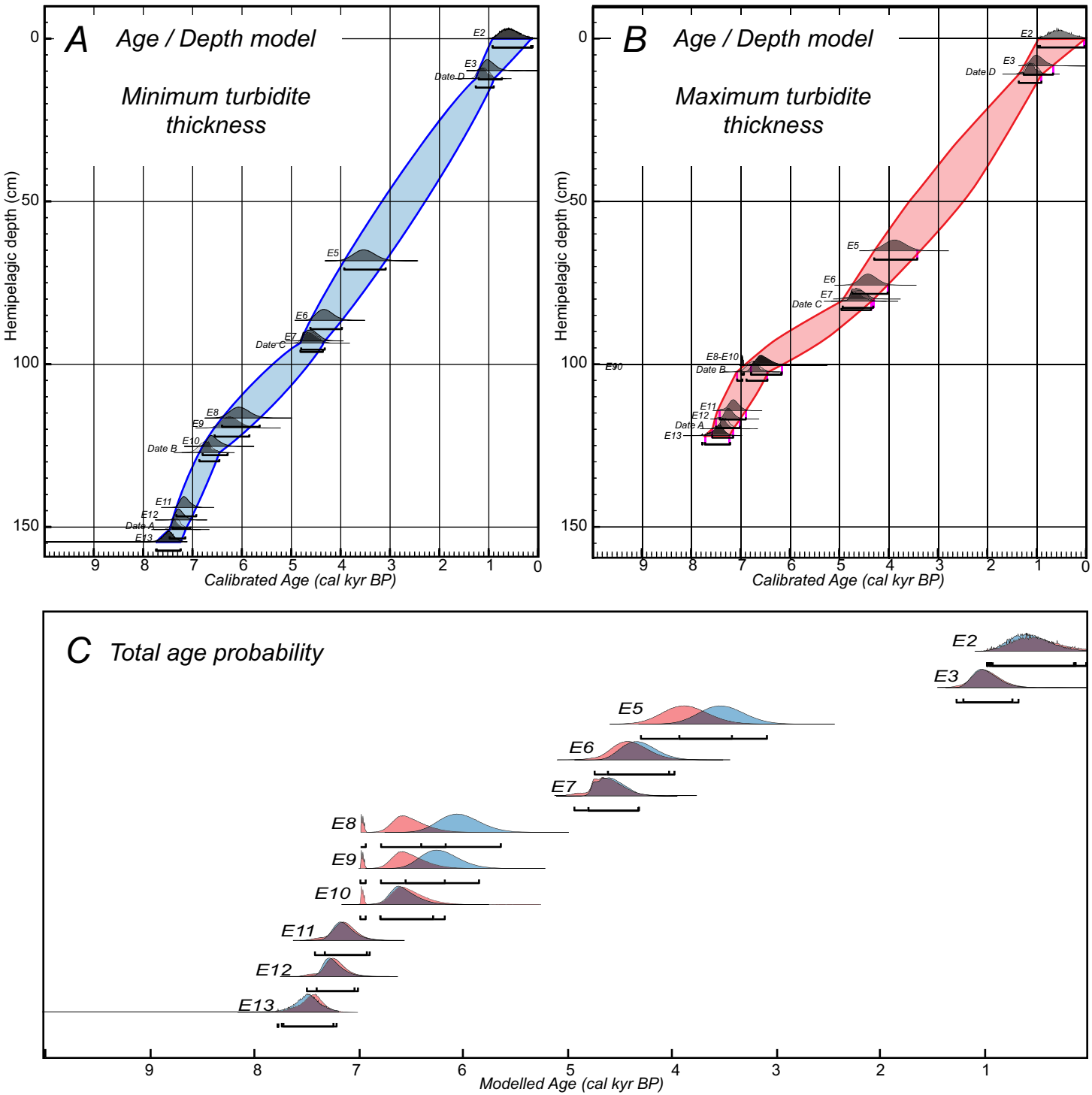
A
Age / Depth model
Minimum turbidite thickness
B
Age / Depth model
Maximum turbidite thickness
Hemipelagic depth (cm)
0
50
100
150
E2
E3
Date D
E5
E6
E7
Date C
E8
E9
E10
Date B
E11
E12
Date A
E13
E8-E10
E90
9
8
7
6
5
4
3
2
1
0
Calibrated Age (cal kyr BP)
C
Total age probability
Modelled Age (cal kyr BP)

KMDJ07

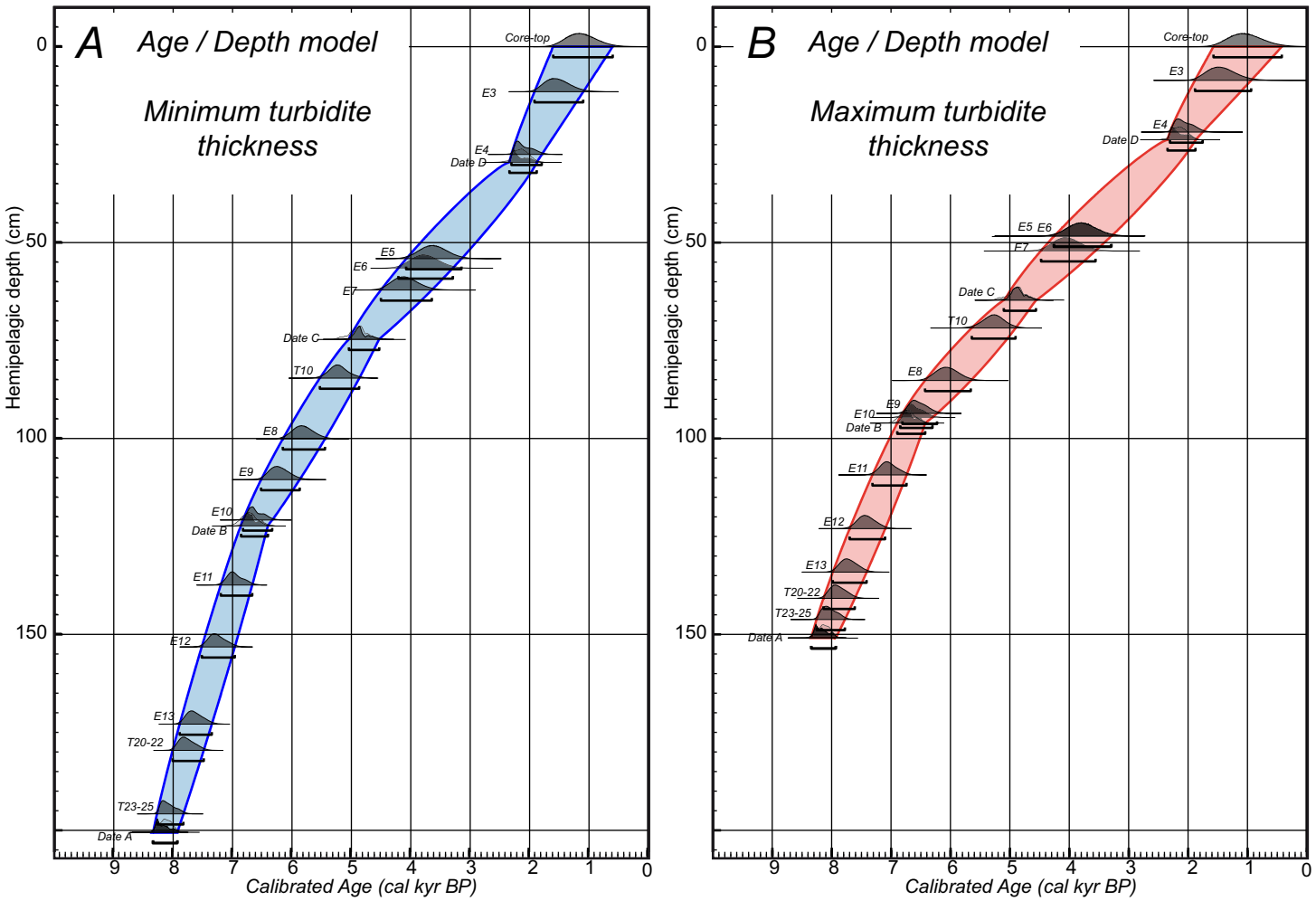
A
Age / Depth model
Minimum turbidite thickness
B
Age / Depth model
Maximum turbidite thickness
Hemipelagic depth (cm)
0
50
100
150
Core-top
E3
E4
Date D
E5
E6
E7
Date C
T10
E8
E9
E10
Date B
E11
E12
E13
T20-22
T23-25
Date A
9
8
7
6
5
4
3
2
1
0
Calibrated Age (cal kyr BP)

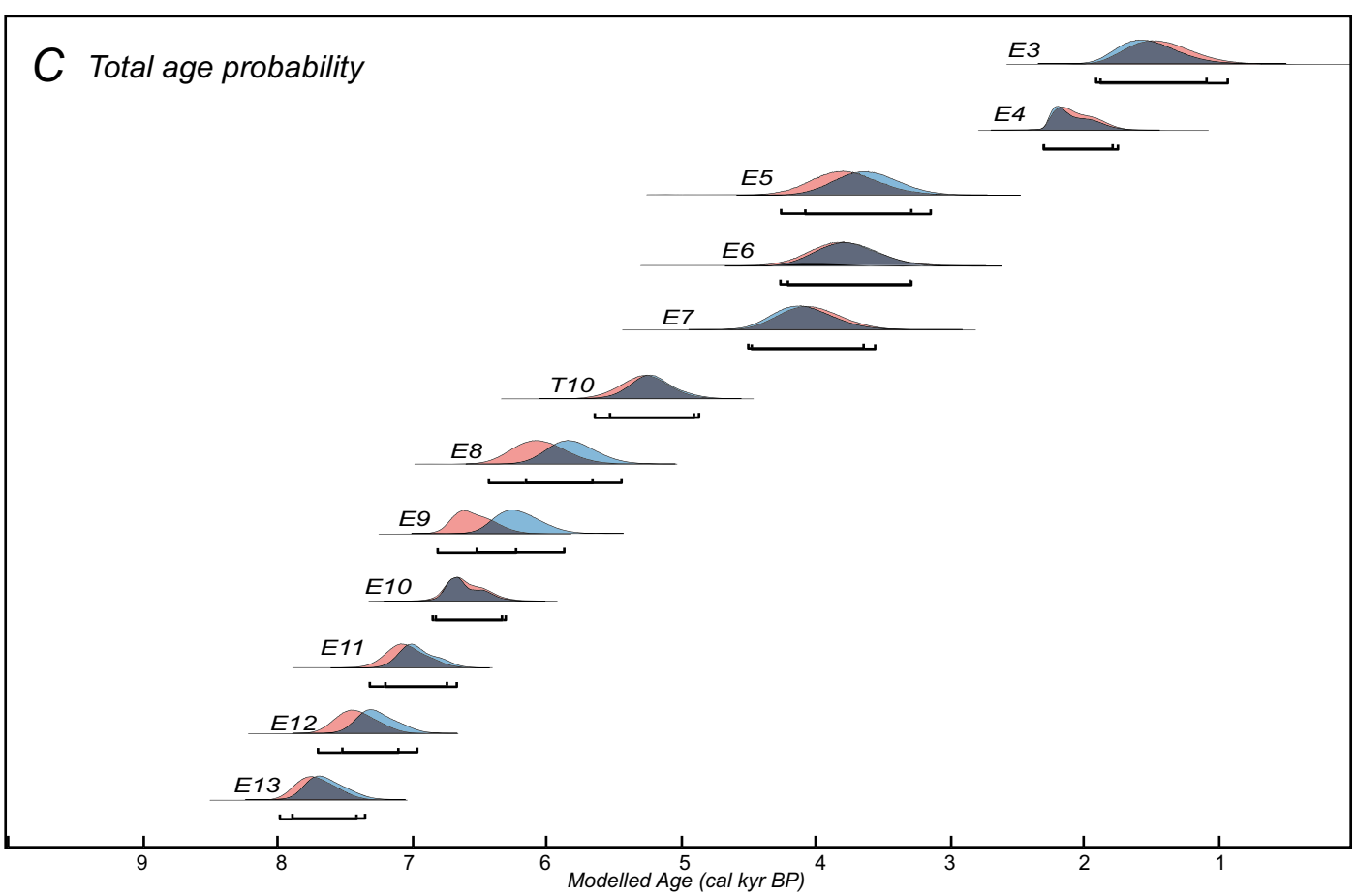
C
Total age probability
E3
E4
E5
E6
E7
T10
E8
E9
E10
E11
E12
E13
9
8
7
6
5
4
3
2
1
Modelled Age (cal kyr BP)

PSMKS19

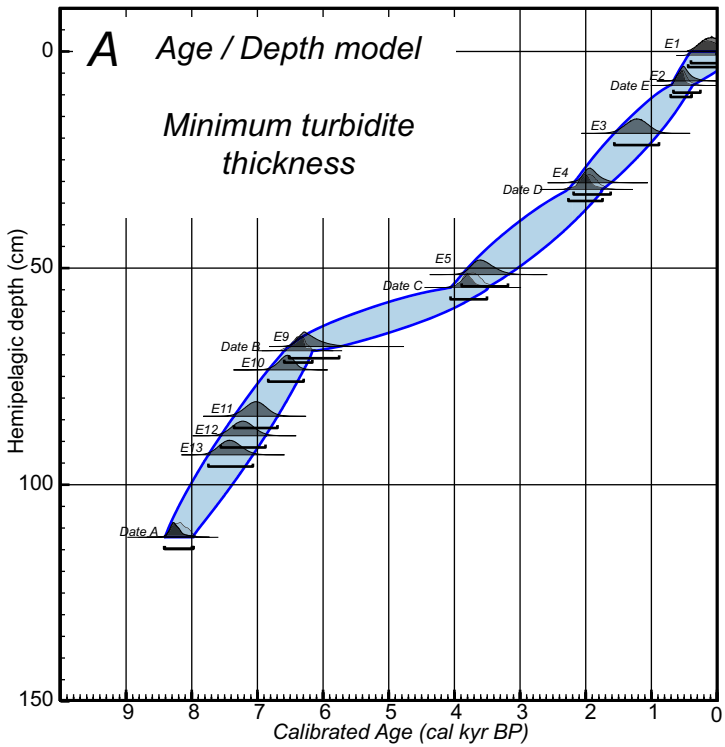
A
Age / Depth model
Minimum turbidite thickness
Hemipelagic depth (cm)
Calibrated Age (cal kyr BP)
Date A
Date B
Date C
Date D
Date E
E1
E2
E3
E4
E5
E9
E10
E11
E12
E13

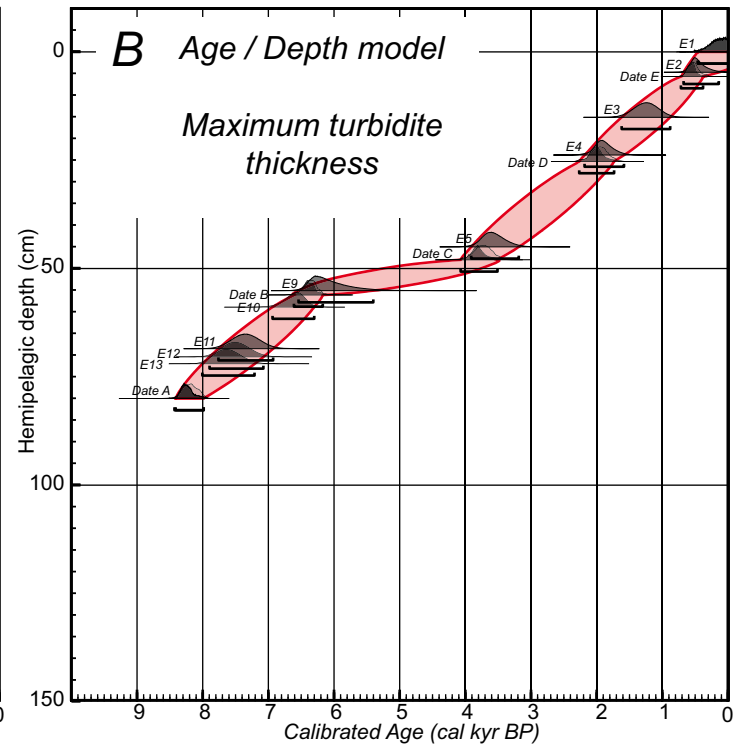
B
Age / Depth model
Maximum turbidite thickness
Hemipelagic depth (cm)
Calibrated Age (cal kyr BP)
Date A
Date B
Date C
Date D
Date E
E1
E2
E3
E4
E5
E9
E10
E11
E12
E13

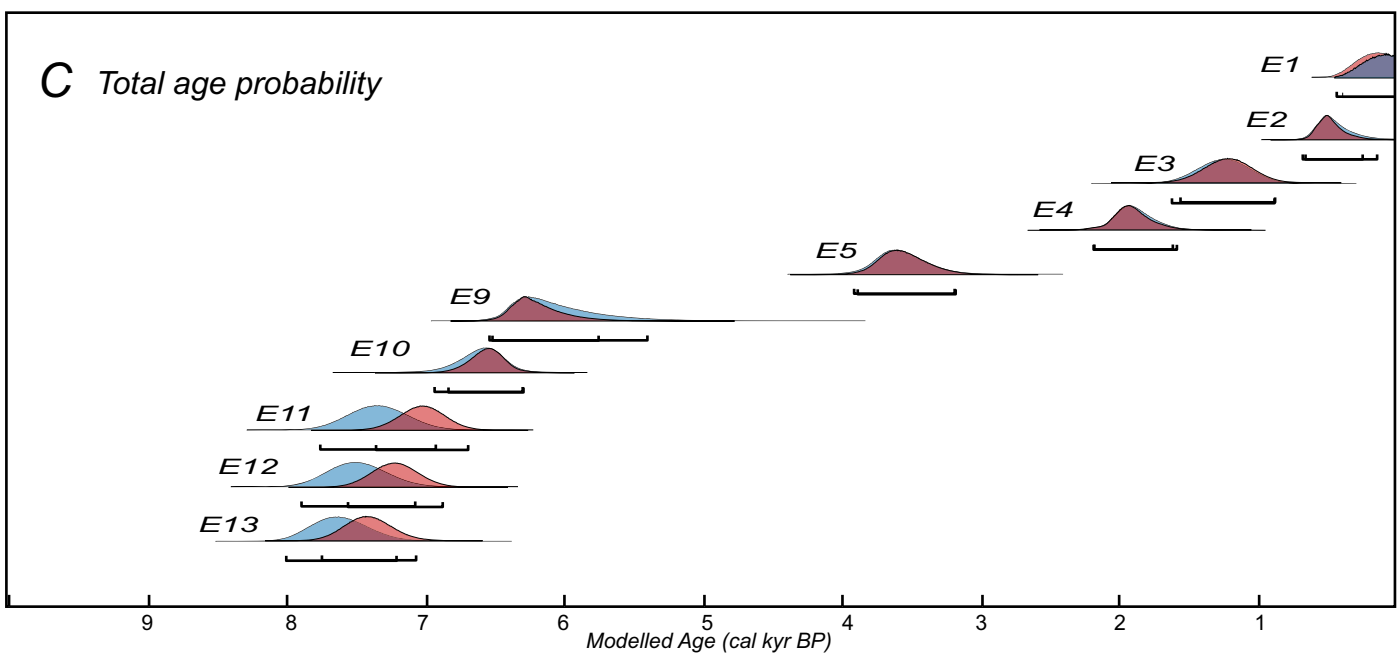
C
Total age probability
Modelled Age (cal kyr BP)
E1
E2
E3
E4
E5
E9
E10
E11
E12
E13

DR8: Peak ground acceleration (PGA±σ) predicted for historical earthquakes using Akkar and Bommer (2010) empirical equations for rock sites and strike-slip earthquakes. The x axe corresponds to the closest distance between the fault activated during the earthquake and the area of submarine canyon heads where sediment turbibity currents likely originate. Color stripes outline mean PGA values and mean PGA+σ predicted for Mw 6.0 and Mw 7.5 earthquakes (Fig. DR8 for further details). The line at PGA=0.1 g depicts the limit above which the slope could fail. Historical earthquakes include: 1522 M~6.9 Almeria (Martinez-Solares and Mezcua, 2002), 1954 Ms6.7 Orléansville (McKenzie, 1972), 1980 Ms7.3 El Asnam (Deschamps et al., 1982), 1989 Mw6.0 Mont Chenoua (Bounif et al, 2003), and 2003 Mw6.8 Boumerdes (Bounif et al., 2004)

According to geotechnical analyses performed on the sediment cover of the Algerian continental slope, slope failures should occur at PGA values larger than 0.1g/0.2g (Dan et al., 2009). Given the distance of the site from the faults, historically, only the 1954 Ms6.7 Orléansville and 1980 Ms7.3 El Asnam, were able to trigger slope failure. However, cable break record proves that only the first did, supporting that the slope was flushed and not enough sediment prone to failure was deposited between the two earthquakes. The 2003 Mw6.8 Boumerdes and 1522 M~6.9 Almeria earthquakes, although of large magnitude are located too far from the studied area, whereas the 1989 Mw6.0 Mont Chenoua earthquake, although coastal had a too low magnitude.

References

Akkar, S., and Bommer, J.J., 2010, Empirical Equations for the Prediction of PGA, PGV, and Spectral Accelerations in Europe, the Mediterranean Region, and the Middle East: Seismological Research Letters, v. 81, p. 195-206.

Bounif, A., Bezzeghoud, M., Dorbath, L., Legrand, D., Deschamps, A., Rivera, L., and Benhallou, H., 2003, Seismic source study of the 1989, October 29, Chenoua (Algeria) earthquake from aftershocks, broad-band and strong ground motion records: Annals of Geophysics, v. 46, p. 625-646.

Bounif, A., Dorbath, C., Ayadi, A., Meghraoui, M., Beldjoudi, H., Laouami, N., Frogneux, M., Slimani, A., Alasset, P., Kherroubi, A., Ousadou, F., Chikh, M., Harbi, A., Larbes, S., and Maouche, S., 2004, The 21 May 2003 Zemmouri (Algeria) earthquake Mw 6.8: Relocation and aftershock sequence analysis: Geophys. Res. Lett., v. 31.

Dan, G., Sultan, N., Savoie, B., Deverchere, J., and Yelles, K., 2009, Quantifying the role of sandy-silty sediments in generating slope failures during seismic shaking: Example from the Algerian margin: International Journal of Earth Sciences, v. 98, p. 769-789.

Deschamps, A., Gaudemer, Y., and Cisternas, A., 1982, The El Asnam, Algeria, earthquake of 10 October 1980: Multiplesource mechanism determined from longperiod records: Bulletin of the Seismological Society of America, v. 72, p. 1111-1128

Martinez-Solares, J.M., and Mézcua, J., 2002, Catálogo Sísmico de la Península Ibérica (880 B.C.-1900 A.D.): Madrid, Monografía No. 18, Instituto Geográfico Nacional, 253 p.

McKenzie, D.P., 1972, Active tectonics of the Mediterranean region: Geophys. J. R. Astron.Soc, v. 30, p. 109-185

Migeon, S., Weber, O., Faugeres, J.C., and Saint-Paul, J., 1999, SCOPIX: a new X-ray imaging system for core analysis: Geo-Marine Letters, v. 18, p. 251-255

Ramsey, C.B., 2008, Deposition models for chronological records: Quaternary Science Reviews, v. 27, p. 42-60.

Reimer, P.J., and McCormac, F.G., 2002, Marine radiocarbon reservoir corrections for the Mediterranean and Aegean Seas: Radiocarbon, v. 44, p. 159-166.

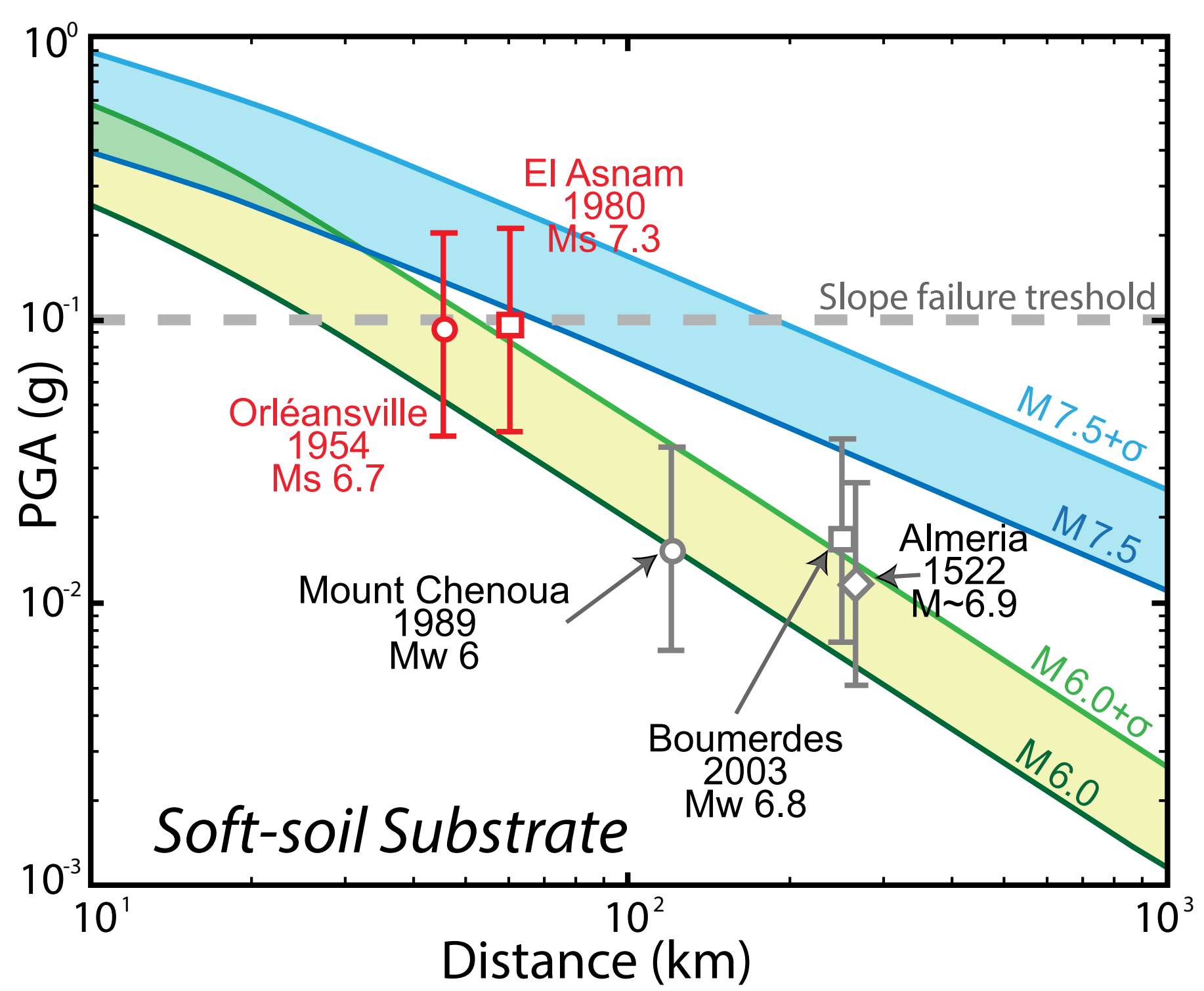
El Asnam
1980
Ms 7.3
Slope failure treshold
Orléansville
1954
Ms 6.7
M7.5+σ
M7.5
Almeria
1522
M~6.9
Mount Chenoua
1989
Mw 6
M6.0+σ
M6.0
Boumerdes
2003
Mw 6.8
Soft-soil Substrate
PGA (g)
Distance (km)
10^0
10^-1
10^-2
10^-3
10^1
10^2
10^3